

Inhibitory mechanism of CRISPR-Cas9 by AcrIIIC4

Xuzichao Li^{1,†}, Fumeng Liao^{1,†}, Jiaqi Gao¹, Guangyong Song¹, Chendi Zhang², Nan Ji¹, Xiaoshen Wang¹, Jing Wen¹, Jia He¹, Yong Wei³, Heng Zhang¹, Zhuang Li^{2,*}, Guimei Yu^{1,*} and Hang Yin^{1,4,*}

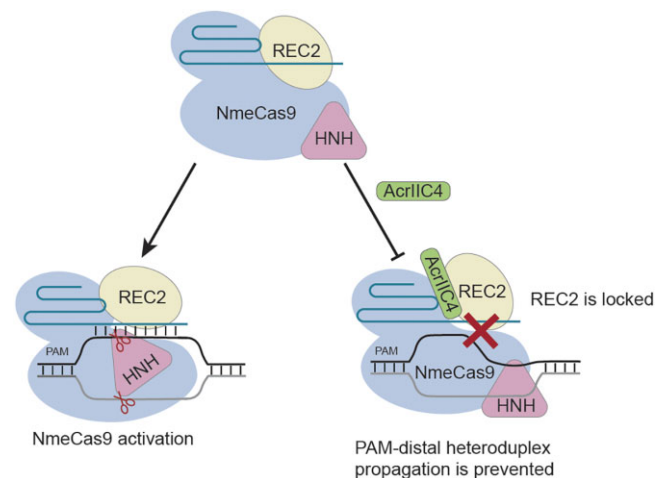
¹State Key Laboratory of Experimental Hematology, Key Laboratory of Immune Microenvironment and Disease (Ministry of Education), The Province and Ministry Co-sponsored Collaborative Innovation Center for Medical Epigenetics, Haihe Laboratory of Cell Ecosystem, Department of Biochemistry and Molecular Biology, School of Basic Medical Sciences, Tianjin Medical University, Tianjin 300070, China, ²State Key Laboratory of Biocatalysis and Enzyme Engineering, School of Life Sciences, Hubei University, Wuhan 430062, China, ³The Cancer Hospital of the University of Chinese Academy of Sciences (Zhejiang Cancer Hospital), Institute of Basic Medicine and Cancer (IBMC), Chinese Academy of Sciences, Hangzhou, China and ⁴Department of Pharmacology, School of Basic Medical Sciences, Tianjin Medical University, Tianjin 300070, China

Received January 04, 2023; Revised July 24, 2023; Editorial Decision July 26, 2023; Accepted August 12, 2023

ABSTRACT

CRISPR-Cas systems act as the adaptive immune systems of bacteria and archaea, targeting and destroying invading foreign mobile genetic elements (MGEs) such as phages. MGEs have also evolved anti-CRISPR (Acr) proteins to inactivate the CRISPR-Cas systems. Recently, AcrIIIC4, identified from *Haemophilus parainfluenzae* phage, has been reported to inhibit the endonuclease activity of Cas9 from *Neisseria meningitidis* (NmeCas9), but the inhibition mechanism is not clear. Here, we biochemically and structurally investigated the anti-CRISPR activity of AcrIIIC4. AcrIIIC4 folds into a helix bundle composed of three helices, which associates with the REC lobe of NmeCas9 and sgRNA. The REC2 domain of NmeCas9 is locked by AcrIIIC4, perturbing the conformational dynamics required for the target DNA binding and cleavage. Furthermore, mutation of the key residues in the AcrIIIC4-NmeCas9 and AcrIIIC4-sgRNA interfaces largely abolishes the inhibitory effects of AcrIIIC4. Our study offers new insights into the mechanism of AcrIIIC4-mediated suppression of NmeCas9 and provides guidelines for the design of regulatory tools for Cas9-based gene editing applications.

GRAPHICAL ABSTRACT



INTRODUCTION

The arms race between prokaryotes and their predators drives their co-evolution (1). Bacteria and archaea have evolved the CRISPR-Cas systems to defend foreign mobile genetic elements (MGEs) such as phages, which are composed of the clustered regularly interspaced short palindromic repeats (CRISPR) arrays and the CRISPR-associated (Cas) effector proteins (2). The CRISPR-Cas systems are currently classified into two classes and six types (3). Among them, the class 2 type II CRISPR-Cas9 system is best characterized and most widely used in gene editing (4). The single Cas9 effector consists of a recognition (REC) lobe and a nuclease (NUC) lobe. Cas9 binds with the

*To whom correspondence should be addressed. Tel: +86 22 83336833; Email: zhuangli@hubu.edu.cn

Correspondence may also be addressed to Guimei Yu. Email: guimei.yu@tmu.edu.cn

Correspondence may also be addressed to Hang Yin. Email: yinhang20@outlook.com

[†]The authors wish it to be known that, in their opinion, the first two authors should be regarded as Joint First Authors.

CRISPR RNA (crRNA) and the trans-activating crRNA (tracrRNA), which could be combined into one molecule named as single guide RNA (sgRNA) (5). The recognition of sgRNA is mediated by the REC lobe, composed of the arginine-rich bridge helix (BH), REC1 and REC2 domains. The protospacer adjacent motif (PAM)-recognition is mediated by the wedge domain (WED) and PAM-interacting domain (PI) within the NUC lobe. After the binding of a DNA sequence complementary to the sgRNA, Cas9 cleaves the target DNA in a sequence-specific way by the two endonuclease domains (HNH and RuvC) in the NUC lobe.

The type II-A Cas9 from *S. pyogenes* (SpyCas9) is the most widely used system in gene editing (6,7). Meanwhile, several orthologs of SpyCas9 with smaller molecular weights, have been characterized as candidates for gene editing (7,8). Among them is the type II-C Cas9 from *N. meningitidis* (NmeCas9), which is 286 amino acids smaller than SpyCas9 (8). The PAM consensus and the spacer-derived guide sequences of NmeCas9 system are longer than those of SpyCas9 system, indicative of a lower off-targeting level, rendering NmeCas9 a promising alternative gene engineering platform (9,10).

In the long course of evolution, phages have evolved anti-CRISPR (Acr) proteins to escape the bacterial CRISPR-Cas systems, which could be utilized to regulate gene editing (11,12). More than 20 type II-A and type II-C Acr proteins have been identified to inhibit the Cas9 systems (13). Structural and biochemical studies on the Acr proteins reveal diverse inhibitory mechanisms. Although the Acr proteins targeting type II-A Cas9 have been extensively explored, only four type II-C Acr proteins (AcrIIC1, AcrIIC2, AcrIIC3 and AcrIIC5) have been well-characterized (14–17). AcrIIC1 binds to the catalytic sites on the HNH domain, conformationally restraining the HNH domain, and thus prevents the target DNA cleavage (15). AcrIIC2 binds to the BH domain and impacts the binding of sgRNA to NmeCas9 (16). Distinctly, AcrIIC3 induces the dimerization of NmeCas9 and locks the HNH domain away from the target DNA cleavage site (9). Moreover, AcrIIC5 mimics DNA and occupies the PAM-binding site, thereby inhibiting the endonuclease activity of NmeCas9 (17).

Recently, AcrIIC4 from the *H. parainfluenzae* phage has been identified to robustly suppress the endonuclease activities of type II-C Cas9 orthologs, including NmeCas9 and HpaCas9 (18). Two recent studies on the inhibitory mechanism of AcrIIC4 have reported contradictory findings (19,20). While Hwang and colleagues observed that neither sgRNA nor target DNA binding is impaired in the presence of AcrIIC4 (20), the other research team reported that AcrIIC4 inhibits NmeCas9 by blocking target DNA binding (19). Additionally, the two studies revealed different crystal structures of AcrIIC4. Therefore, to further elucidate the inhibition mechanism of AcrIIC4, we solved the structures of AcrIIC4 alone, and the full-length NmeCas9-sgRNA-AcrIIC4 ternary complex. Combined with mutagenesis and biochemical studies, we reveal that AcrIIC4 inhibits NmeCas9 mainly by trapping the REC2 domain. The interactions between AcrIIC4 and NmeCas9-sgRNA complex lock the REC2 domain, thereby impairing the conformational dynamics of NmeCas9 for target DNA binding and cleavage. This inhibition mechanism of AcrIIC4 differs

from those previously reported for Acr proteins, broadening the insights into the diversity of Acr proteins and providing a basis for the development of the Cas9 inhibitors for applications.

MATERIALS AND METHODS

Protein expression and purification

Plasmid encoding the full-length NmeCas9 was obtained from Addgene (#71474). The gene encoding AcrIIC4, and NmeCas9-REC2 domain were synthesized in Azenta and inserted into pET15-MHL and pET28-MHL vectors for protein expression and purification. Sequence encoding a 135 nt sgRNA was inserted into 13S-A vector (Addgene: 48323). The plasmids encoding NmeCas9 and sgRNA were co-transformed into *Escherichia coli* BL21 (DE3) cells. The other recombinant plasmids were independently transformed into *E. coli* BL21 (DE3) and 0.2 mM isopropyl β -D-1-thiogalactoside (IPTG) was added for the induction of protein expression at 16°C. Cells were harvested and resuspended in the lysis buffer (20 mM Tris-HCl pH 7.5, 400 mM NaCl, 2 mM β -mercaptoethanol) and lysed by sonication. The lysate was clarified by centrifugation at 14 000 rpm for 40 min. The supernatant was incubated with the Ni-NTA beads (QIAGEN) for 1 h at 4°C, which were then rinsed using the lysis buffer supplemented with 25 mM imidazole. Target protein was eluted by the elution buffer (20 mM Tris-HCl pH 7.5, 400 mM NaCl, 300 mM imidazole pH 7.5, 2 mM β -mercaptoethanol). The fusion tags were then removed by TEV. Proteins were further purified with heparin-Sepharose column (Cytiva) and the size-exclusion chromatography (Superdex increase 200 10/300 GL, Cytiva) with the gel filtration buffer (20 mM Tris-HCl pH 7.5, 300 mM NaCl, 1 mM DTT). For electron microscopy, the NmeCas9-sgRNA ribonucleoprotein and AcrIIC4 complexes were assembled at a molar ratio of 1:5 and further purified by size-exclusion chromatography with the gel filtration buffer.

Protein crystallization

Purified AcrIIC4 were crystallized by the sitting-drop vapor diffusion method at 18°C by mixing 1 μ l of protein sample and 1 μ l of the reservoir buffer. 1 μ l AcrIIC4 protein solution (13.6 mg/ml) was mixed with 1 μ l crystallization buffer containing 0.2 M Sodium malonate pH 7.0 and 20% w/v Polyethylene glycol 3350 (Index kit). The crystals were cryo-protected in the crystallization buffer containing 20% glycerol and flash-frozen in liquid nitrogen for data collection.

Data collection and structure determination

All the X-ray diffraction data sets were collected at beam line BL17U in Shanghai Synchrotron Radiation Facility (SSRF) and processed with autoPROC (21–23). All images were collected at the wavelength of 0.979 Å with 0.5° rotation. All diffraction data sets were processed by HKL3000 (24) and optimized by PHENIX (25). Phase determination was performed by molecular replacement using the model predicted from AlphaFold2 (26). Coot

and phenix.refine were used to further optimize the structural model (27,28). Structural figures were prepared with PyMOL (<https://pymol.sourceforge.net/>). Data collection and refinement statistics are summarized in Supplementary Table S1.

Electron microscopy

Aliquots of 4 μ l samples (0.5 mg/ml for NmeCas9-sgRNA-AcrIIC4 complex) were applied to glow-discharged Quantifoil holey carbon grids (Cu, R1.2/1.3, 300 mesh). The grids were blotted with force 2 for 7 s and plunged into liquid ethane using VitroBot. Cryo-EM data were collected with a Titan Krios microscope (FEI) operated at 300 kV and images were collected using EPU (29) at a nominal magnification of 105 000 \times (resulting in a calibrated physical pixel size of 0.85 Å/pixel) with a defocus range from $-1.2 \mu\text{m}$ to $-2.2 \mu\text{m}$. The images were recorded on a K3 summit electron direct detector in super-resolution mode at the end of a GIF-Quantum energy filter operated with a slit width of 20 eV. A dose rate of 15 electrons per pixel per second and an exposure time of 2.5 s were used, generating 40 movie frames with a total dose of ~ 54 electrons/Å². A total of 1231 movie stacks were collected.

Cryo-EM data of NmeCas9-sgRNA-AcrIIC4 ternary complex were processed using RELION-3 (30). Movie frames were aligned using MotionCor2 (31) with a binning factor of 2. Contrast transfer function (CTF) parameters were estimated using Gctf (32). 547563 particles were auto-picked without template and extracted from the dose weighted micrographs. 2D classification was performed to exclude false and bad particles that fall into 2D averages with poor features. 251 996 particles were selected for further processing. Particles from different views were used to generate initial model in cryoSPARC (33). 3D classification was performed to distinguish different conformational states via cryoSPARC. 165 351 particles were used for final 3D refinement in cryoSPARC, converging at 3.5 Å resolution.

Details of the cryo-EM image processing is summarized in Supplementary Table S2.

In vitro transcription and purification of sgRNA

The template dsDNA of sgRNA was amplified by PCR and then transcribed *in vitro* with homemade T7 RNA polymerase. Transcription reactions (1 ml) were performed in the buffer containing 0.1M HEPES-K pH 7.9, 12 mM MgCl₂, 30 mM DTT, 2 mM spermidine, 2 mM NTPs, 80 μ g/ml T7 RNA polymerase and 32 μ g/ml transcription template at 37°C. sgRNA was purified by gel electrophoresis on 8% denatured (8 M urea) polyacrylamide gel and then extracted overnight by RNA elute buffer (200 mM NaCl, 1 mM EDTA). Finally, the sgRNA was resuspended in the DEPC-H₂O and stored at -80°C for subsequent use.

In vitro DNA cleavage assay

Target DNA sequences containing the 5'-GATT-3' PAM motif were cloned into pET28-MKH8SUMO vector, and then linearized with FspI (NEB). NmeCas9, sgRNA and

AcrIIC4 were diluted with the cleavage buffer (25 mM Tris-HCl pH 7.5, 200 mM KCl, 5 mM MgCl₂, 5 mM DTT, 5% glycerol). To test the inhibitory activity of the AcrIIC4 proteins, 150 nM NmeCas9, sgRNA and AcrIIC4 were incubated in the cleavage buffer in order as indicated in Figure 1A, followed by adding of 200 ng target DNA. Molar ratios of NmeCas9-AcrIIC4 ranging from 1:5 to 1:100 were used in Supplementary Figure S1B. The cleavage assay was incubated at 37°C for 15 min at each step and stopped by adding 40 mM EDTA and 1 mg/ml protease K at 37°C for 15 min. The reaction products were analyzed by 0.5% TBE agarose gel with SYBR Safe stain (Thermo Fisher Scientific).

Electrophoretic mobility shift assay (EMSA)

For the EMSA assays, purified NmeCas9 protein was incubated with sgRNA in the molar ratio of 2:1 in the cleavage buffer, and then verified by sgRNA dissociation experiment. DNA for EMSA was labeled with 6-carboxyfluorescein (FAM) at the 5' end of non-target sequence. The sequences for DNA EMSA are NTS 5'-ACTTCAGGTCACTCTGCTATTTAACTTTACATATGATTTTA-3' and T S 5'-TAAATCATATGTAAAGTTAAATAGCAGAGTGACCTGAAGT-3'. The incubation of reaction components was the same as the above target DNA cleavage experiment. Samples were loaded onto a 6% native PAGE and the gel run for 40 min at 120 V at 4°C. The gels were visualized by the SYBR Safe stain (Thermo Fisher Scientific).

Size-exclusion chromatography assay

Size-exclusion chromatography assay was performed using the Superdex increase 200 10/300 GL column (Cytiva). NmeCas9 or the REC2 domain was mixed with AcrIIC4 at a molar ratio of 1:3 and incubated on ice for 40 min. Then the protein mixture was loaded onto the gel filtration column pre-equilibrated with the gel filtration buffer (20 mM Tris-HCl pH 7.5, 300 mM NaCl, 1 mM DTT). Samples of peak fractions were analyzed by SDS-PAGE.

His pull-down assay

His-tagged NmeCas9 (WT and truncations) proteins and RNPs (WT and mutants) were first incubated with Ni-NTA resin in binding buffer containing 20 mM Tris-HCl pH 7.5, 300 mM NaCl and 2 mM β -mercaptoethanol at 4°C for 30 min. Tag-free AcrIIC4 proteins (WT and mutants) were then added and incubated for another 1 h. The resin was washed 3 times with 1ml binding buffer supplemented with 20 mM imidazole, and samples were eluted with binding buffer supplemented with 500 mM imidazole. The results were analyzed by SDS-PAGE and visualized with Coomassie Blue staining.

RESULTS

AcrIIC4 inhibits NmeCas9-mediated DNA cleavage

To characterize the inhibition mode of AcrIIC4 on NmeCas9, we performed the NmeCas9-mediated DNA cleavage assay in the absence or presence of AcrIIC4 with different assembly orders (Figure 1A). Guided by the

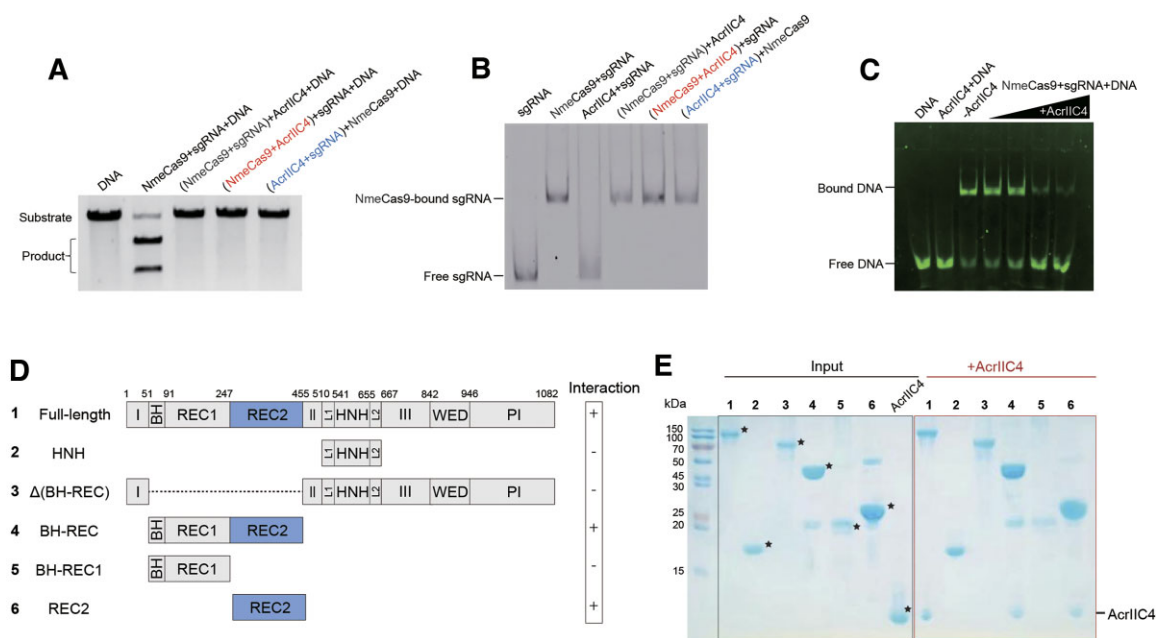


Figure 1. AcrIIC4 inhibits the NmeCas9-mediated target DNA cleavage. (A) *In vitro* DNA cleavage assays of NmeCas9 in the presence or absence of AcrIIC4. The experiments were performed with different assembly orders, and each experiment was repeated three times. (B) RNA electrophoretic mobility shift assays (EMSA) using catalytically inactive dNmeCas9 in the presence of AcrIIC4. The experiments were conducted using different assembly orders, as described in Figure 1A. Three independent replicate experiments were conducted. (C) DNA electrophoretic mobility shift assays (EMSA) in the presence or absence of AcrIIC4. The experiments were independently replicated three times. (D, E) His pull-down assay of AcrIIC4 with full-length and truncation mutants of NmeCas9.

sgRNA, NmeCas9 could cleave target DNA into two fragments, while the endonuclease activity of NmeCas9 was prevented when AcrIIC4 was added, confirming the robust inhibitory effect of AcrIIC4 on NmeCas9. Further, the NmeCas9-mediated target DNA cleavage was inhibited by AcrIIC4 regardless of the assembly order (Figure 1A), consistent with a previous study (34). To examine whether AcrIIC4 could affect sgRNA binding or target DNA binding, we performed the gel electrophoresis mobility shift assay (EMSA). Compared to the band corresponding to free sgRNA, a slow-migrating band was observed in the presence of NmeCas9 in EMSA, indicative of the NmeCas9-sgRNA ribonucleoprotein (RNP) complex formation (Figure 1B). AcrIIC4 had no obvious effect on the migration of sgRNA regardless of the assembly order, even when the concentrations of AcrIIC4 were increased (Figure 1B, Supplementary Figure S1A), indicating that AcrIIC4 does not impair sgRNA binding to NmeCas9. We next investigated the effects of AcrIIC4 on target DNA binding using the catalytically inactive NmeCas9 in EMSA. The results showed that AcrIIC4 blocks target DNA binding in a concentration-dependent manner (Figure 1C). Likewise, the NmeCas9 endonuclease activity was concentration-dependently prevented by AcrIIC4 (Supplementary Figure S1B).

AcrIIC4 binds to the REC2 domain of NmeCas9

To further dissect the inhibitory mechanism of AcrIIC4, we next characterized the interactions between AcrIIC4 and NmeCas9. AcrIIC4 eluted between 1.35 kDa and 17

kDa in the size-exclusion chromatography (SEC) assay, suggesting a monomeric state in solution (Supplementary Figure S1C). Additionally, we found AcrIIC4 co-eluted with NmeCas9 in the gel filtration, indicating a direct association between AcrIIC4 and NmeCas9 (Supplementary Figure S1D). To identify the region of NmeCas9 interacting with AcrIIC4, we generated a series of truncations and performed the pull-down assay (Figures 1D, E). Apart from the full-length NmeCas9, only truncants containing the REC2 domain could pull down AcrIIC4 (Figure 1E), implying that the REC2 domain may be responsible for AcrIIC4 binding. Consistently, the purified REC2 domain-only protein co-migrated with AcrIIC4 in the SEC assay (Supplementary Figure S1E). Therefore, these results indicate that AcrIIC4 may inactivate NmeCas9 by specifically binding to the REC2 domain.

Structures of AcrIIC4 in complex with NmeCas9

We next attempted to solve the structures of AcrIIC4 alone and in complex with NmeCas9. We first crystallized AcrIIC4 and determined its crystal structure at a resolution of 1.8 Å. Almost all the residues of AcrIIC4 were clearly traced in the electron density map, and an asymmetric unit contains four AcrIIC4 molecules (Supplementary Figure S2A). The four molecules are nearly identical to each other (Supplementary Figure S2B). AcrIIC4 folds into an α -helical bundle, consisting of one short helix (α 1) and two long helices (α 2- α 3), reminiscent of the previously reported structures (19,20) (Supplementary

Figure S2A–C). We further reconstituted the NmeCas9-sgRNA-AcrIIC4 ternary complex (Figures 2A–B), and determined its cryo-EM structure at a resolution of 3.5 Å (Figures 2C–D, Supplementary Figure S3). The high-quality cryo-EM density allowed model building for NmeCas9 and AcrIIC4 except for several loop regions of NmeCas9 (residues 114–155, 331–341, 711–719, 750–770). The majority of sgRNA, including the stem loops 1–2, repeat:anti-repeat duplex and the seed region, were also well resolved. However, densities corresponding to the 5'-end of the spacer region in sgRNA were not well defined, possibly due to flexibility (Figure 2C, Supplementary Figure S3H). AcrIIC4 binds to RNP at a stoichiometry of 1:1, with one AcrIIC4 inserted into the REC lobe and sgRNA (discussed below). Compared to the apo AcrIIC4, the binding to RNP does not alter the overall structure of the AcrIIC4 (Supplementary Figure S2C).

Interaction between AcrIIC4 and NmeCas9

Nearly half of the $\alpha 2$ - $\alpha 3$ helices of AcrIIC4 (aa 35–61), termed the upper half, are sandwiched between the REC1 and REC2 domains (Figure 3A). AcrIIC4 makes extensive contacts with REC2, consistent with our pull-down assays showing that the REC2 domain primarily mediates the interactions with AcrIIC4 (Figures 1D–E). In particular, the side chains of Lys50, Glu52, and Asn63 in AcrIIC4 form polar interactions with Ser416, Lys362 and Lys390 from the REC2 domain, respectively (Figure 3B). Notably, Arg46 of AcrIIC4 is buttressed by Lys390, Asp392 and Ile415 from REC2 domain, indicative of the importance of Arg46 (Figure 3B). Indeed, alanine substitution of Arg46 not only abrogated the interactions between AcrIIC4 and NmeCas9 (Supplementary Figure S4A), but also failed to inhibit the NmeCas9-mediated target DNA cleavage (Figure 3C). Importantly, our results agree well with the previous *in vivo* phage targeting assay showing that R46A mutation reduces the anti-CRISPR activity of AcrIIC4 (20). Intriguingly, Phe49 is responsible for coordinating Arg46 in our ternary complex structure (Supplementary Figure S4B). Given the critical role of Arg46, it is reasonable to expect that Phe49 may be important for the anti-CRISPR activity of AcrIIC4. As anticipated, F49A mutation is also reported to compromise the anti-CRISPR function of AcrIIC4 both *in vitro* and *in vivo* (20). Besides the polar interactions, hydrophobic contacts are also found in the REC2-binding interface. For instance, a hydrophobic cluster comprising residues Ala250, Val251 and Met254 from REC2 domain packs into the $\alpha 1$ - $\alpha 2$ interface groove of AcrIIC4, which is created by Phe17, Phe35, Lys36 and Val39 (Figure 3B). The interaction of AcrIIC4 with NmeCas9 was disrupted by mutation of the hydrophobic residues (F35A/V39G) in AcrIIC4 (Supplementary Figure S4A). As expected, this double mutation was incapable of suppressing the NmeCas9 activity (Figure 3C). The REC1 domain is accommodated by a hydrophobic patch of AcrIIC4 with a relatively smaller interface (Supplementary Figure S4C). Mutation of the hydrophobic patch also reduced the inhibition of NmeCas9 by AcrIIC4 (Figure 3C), although the interactions between them appeared to be largely unaffected (Supplementary Figure S4A), suggesting that the structural integrity of AcrIIC4 is critical

for inhibiting NmeCas9. In parallel, we generated mutations in NmeCas9 to examine our structural model by pull-down assays. Mutations of the key residues in NmeCas9 also disrupted the AcrIIC4-NmeCas9 interactions (Supplementary Figure S4D), further confirming our structural observations.

Interaction between AcrIIC4 and sgRNA

Surprisingly, in addition to the binding of NmeCas9, AcrIIC4 is also found to engage sgRNA. The lower half of the AcrIIC4 helix bundle is bracketed by the stem loop 1 and stem loop 2 of sgRNA (Figure 3A). In contrast to a mixture of polar and hydrophobic contacts between AcrIIC4 and NmeCas9, the electrostatic interactions appear to predominantly mediate the AcrIIC4-sgRNA association, as a positively charged surface of AcrIIC4 is exposed to the juxtaposed stem loop 1 and stem loop 2 (Supplementary Figure S4E). Two positively charged residues (Lys25 and Arg28) in $\alpha 2$ of AcrIIC4 form salt bridges with the phosphate backbones from stem loop 2 (Figure 3D). Likewise, a salt bridge is also established between stem loop 1 and AcrIIC4 through Lys73 in $\alpha 2$ (Figure 3D). Mutation of these residues (K25A/R28A and K73G) in the AcrIIC4-sgRNA interface led to the dissociation of AcrIIC4 from the RNP and the loss of the inhibitory activity of AcrIIC4 (Figure 3C, Supplementary Figure S4A), further underscoring the importance of electrostatic contacts in the recognition of sgRNA by AcrIIC4. Notably, the flipped-out 84U from stem loop 1, which is coordinated by a positively charged residue (Arg81 from BH), forms a hydrogen bond with Glu65 of AcrIIC4 (Figure 3D). Nevertheless, E65G mutations had little impact on the function of AcrIIC4 (Figure 3C, Supplementary Figure S4A). Apart from the edge-mediated contacts with AcrIIC4, $\alpha 2$ and $\alpha 3$ helices from AcrIIC4 stack tightly against the groove of stem loop 1. For example, Glu29 is hydrogen bonded to the guanine base of 68G from stem loop 1 (Figure 3D). However, the E29A mutation had no discernible effect on AcrIIC4 (Figure 3C, Supplementary Figure S4A).

The target DNA binding is influenced by REC2 domain in the presence of AcrIIC4

To elucidate the molecular mechanism by which AcrIIC4 inhibits the NmeCas9-mediated target DNA cleavage, we compared our AcrIIC4-bound NmeCas9 structure with previously solved NmeCas9 structures, including the NmeCas9-sgRNA binary complex (RNP), seed-paired NmeCas9-sgRNA-dsDNA ternary complex (seed-paired state) and fully paired NmeCas9-sgRNA-dsDNA ternary complex (catalytic state) (35). The overall structure of AcrIIC4-bound complex is similar to that of the RNP complex, with the exception of the REC2 domain (Supplementary Figure S5A). In particular, the REC2 domain undergoes a ~ 20 Å outward movement upon AcrIIC4 binding, leading to the widening of the channel between the REC and NUC lobes. However, the PAM-distal end of this channel narrows. Together, it is plausible that the PAM-proximal, but not the PAM-distal, sgRNA-DNA duplex could be formed in the presence of AcrIIC4. As anticipated,

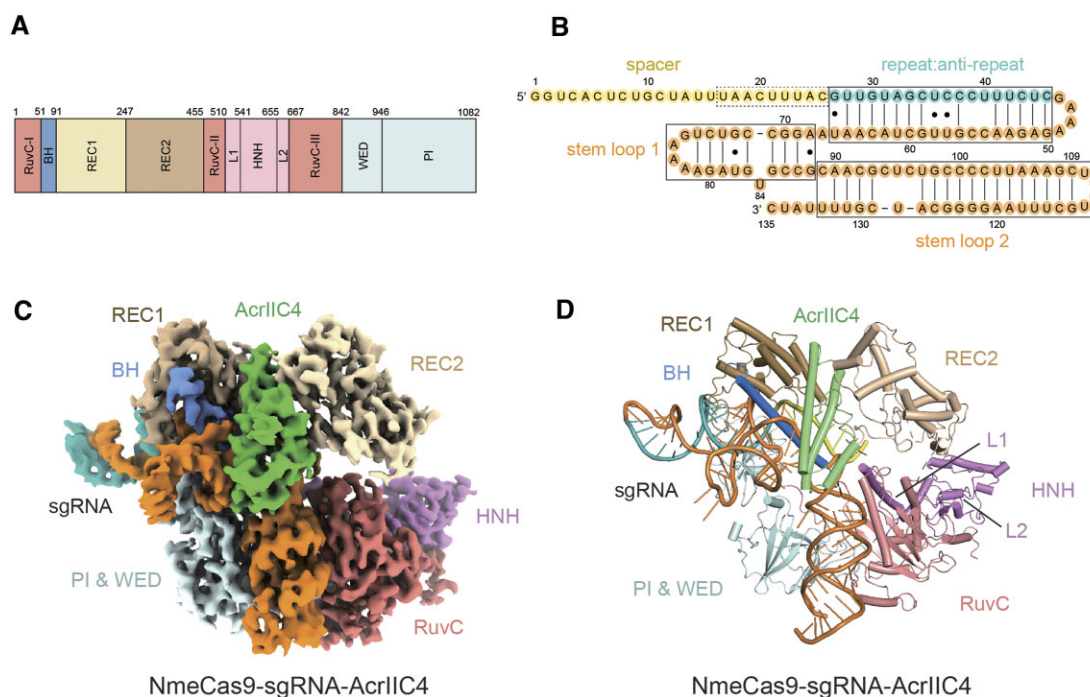


Figure 2. Cryo-EM structure of NmeCas9-sgRNA-AcrIIC4 ternary complex. (A) Domain organization of NmeCas9. (B) Schematic diagram of the resolved sgRNA. (C) Cryo-EM density map of NmeCas9-sgRNA-AcrIIC4 ternary Complex. The AcrIIC4 is colored green. The RuvC, BH, REC1, REC2, HNH, WED and PI domains of NmeCas9 are colored in pink, blue, brown, wheat, violet and pale cyan, respectively. The density map of repeat and spacer regions of sgRNA is shown in yellow and cyan, and the density of tracrRNA is colored in orange. (D) Atomic model of NmeCas9-sgRNA-AcrIIC4 ternary complex. The model is shown in the same color scheme as in (C).

the 8 nt seed-matched heteroduplex in the seed-paired structure could be docked into this PAM-proximal channel without introducing steric clashes when superposing the seed-paired structure onto the AcrIIC4-bound structure (Supplementary Figure S5B). A similar scenario is also seen when aligning the catalytic state structure with the AcrIIC4-bound structure (Figures 4A-B). Moreover, AcrIIC4 exhibited minimal impact on the binding of target DNA to NmeCas9 in cases where the target strand (TS) of the target DNA was shorter than 10 nucleotides (Figure 4C).

Nonetheless, structural comparisons revealed that the REC2 domain of NmeCas9 would have substantial clashes with the PAM-distal duplex in the presence of AcrIIC4 (Figure 4B). Particularly, the REC2 domain in the AcrIIC4-bound state substantially overlaps with the 14–20 bp of the duplex in the catalytic state. Consistent with the structural findings, the interaction between NmeCas9 and target DNA carrying a 15–20 nucleotides TS sequence complementary to the sgRNA was compromised by AcrIIC4 (Figure 4C). Altogether, these results demonstrate that AcrIIC4 decreases, but does not abolish, the binding of target DNA to RNP.

AcrIIC4 inactivates NmeCas9 by locking the REC2 domain

The PAM-distal base pairing between sgRNA and target DNA facilitates the conformational changes of NmeCas9, especially the REC2 and HNH domains, which are required to activate NmeCas9 (35). Our *in vitro* cleavage assays further showed that the NmeCas9-mediated target DNA cleavage was almost abolished when the TS strand is less than

18 nt complementary to sgRNA (Supplementary Figure S6), which agrees well with the previous *in vivo* experiments (10). As aforementioned, the PAM-distal heteroduplex propagation is expected to be prevented by the REC2 domain in the presence of AcrIIC4. It is reasonable to suggest that the interrupted base pairing between sgRNA and target DNA may, at least partially, lead to the inactivation of NmeCas9. More importantly, the outward movement of the REC2 domain is proposed to induce the rearrangement of the HNH domain, thus eliciting the endonuclease activity of NmeCas9 (35). Nonetheless, the REC2 domain is tightly locked by AcrIIC4, without the potential for conformational change. The linker region bridging the HNH and RuvC domains is thought to interact with the sgRNA-DNA heteroduplex, especially the PAM-distal segment (35). Additionally, the conformational rearrangement of these linker regions is crucial for the correct positioning of catalytic domains (36,37). However, steric clashes are observed between the linker region and REC2 domain when aligning the AcrIIC4-bound structure with the catalytic state structure (Figure 4B). Taken together, it is conceivable that AcrIIC4 inhibits the endonuclease activity of NmeCas9 mainly by perturbing the necessary conformational dynamics of REC2 domain.

DISCUSSION

Anti-CRISPR (Acr) proteins have been evolved by phages to counteract CRISPR-mediated immune response. In this study, we conducted biochemical and structural investigations to examine the inhibition mechanism of NmeCas9

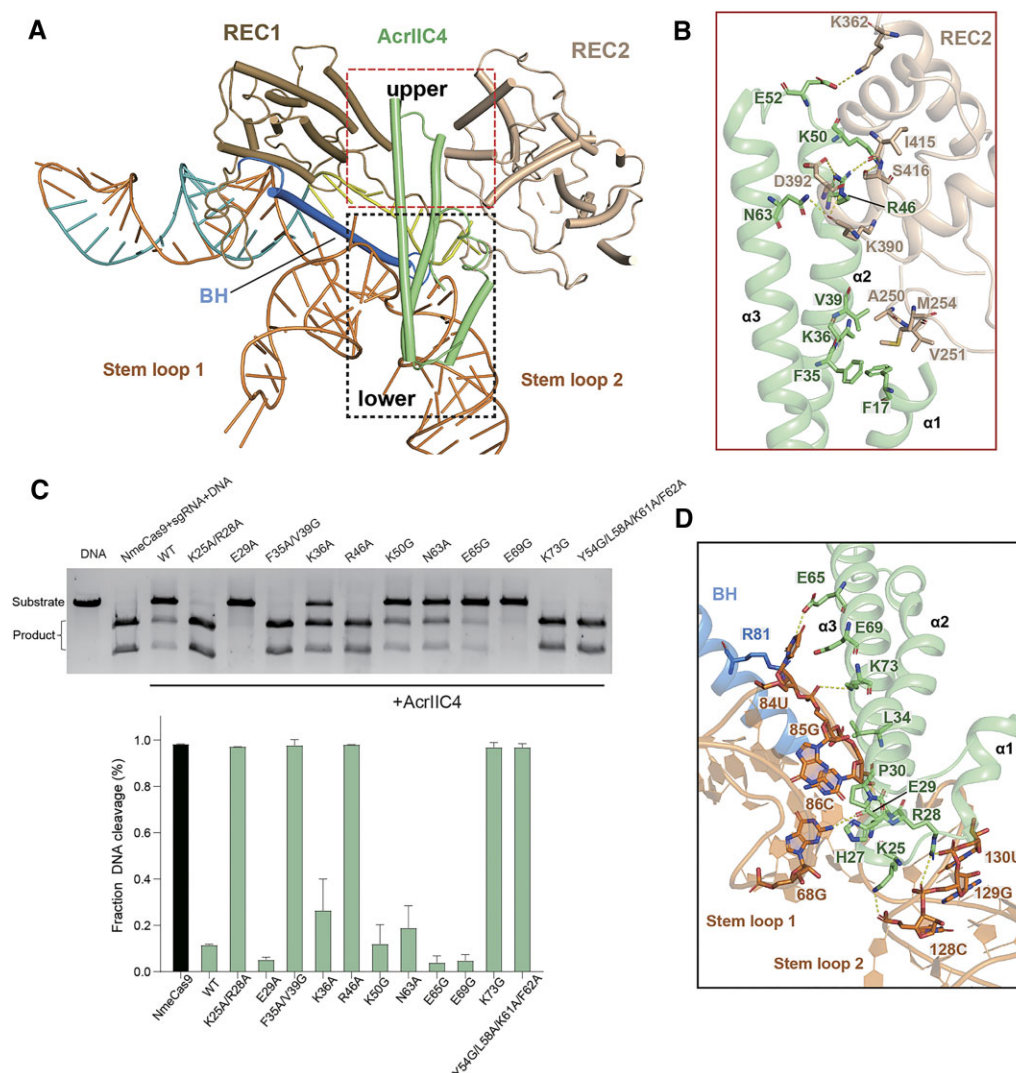


Figure 3. Interactions between AcrIIC4 and NmeCas9-sgRNA binary complex (RNP). (A) Interactions between AcrIIC4 and NmeCas9-sgRNA ribonucleoprotein. The upper half of AcrIIC4 is nestled between the REC1 and REC2 domains (red box), while the lower half of AcrIIC4 is enclosed by stem loop 1 and stem loop 2 of sgRNA (black box). (B) Close-up view of the interactions between the REC2 domain and AcrIIC4, with key interacting residues depicted in stick representation. (C) *In vitro* DNA cleavage assays of NmeCas9 in the presence of wild-type (WT) or mutated AcrIIC4 (upper panel). Mutants of key residues involved in NmeCas9 binding or sgRNA binding are utilized for the DNA cleavage assays. The gel presents the results obtained from three experimental replicates. A bar graph quantifies the band brightness, allowing for clear visualization of the ratios of cleaved product to the substrate (lower panel). (D) Detailed insights into the AcrIIC4-sgRNA binding interface, key interacting residues are shown in stick representation.

by AcrIIC4. Our findings revealed an unexpected interaction mode in which AcrIIC4 inserts into both the REC lobe and sgRNA. Two apo AcrIIC4 structures have previously been reported, but they display different conformations (35). One potential explanation is the crystallization condition, such as the pH of crystallization buffer. One structure, crystallized at pH 8.0, displays a helical bundle architecture (19), while the other structure, crystallized at pH 4.0, shows a long extended helical structure (20) (Supplementary Figure S2C). Supporting this hypothesis, the structure of AcrIIC4 resolved in our study at pH 7.0 closely resembles the structure previously determined at pH 8.0 (Supplementary Figure S2C). Therefore, it seems that AcrIIC4 might undergo pH-sensitive conformational rearrangements. However, further studies will be needed to explore the correlation between the conformations of AcrIIC4 and pH values.

The REC1 and REC2 domains clamp one half of AcrIIC4, while the other half of AcrIIC4 is accommodated in the juxtaposition of sgRNA (Figure 3A). Interestingly, AcrVA4 is also reported to engage both the Cas12a and crRNA (17,38,39). However, AcrVA4 mainly interacts with WED domain rather than REC2 domain. On the other hand, AcrVA4 is anchored to the periphery of crRNA, which is distinct from the observation that AcrIIC4 is inserted into sgRNA. Furthermore, AcrVA4 interacts with Cas12a in a crRNA-dependent fashion, whereas AcrIIC4 could physically bind to NmeCas9 in the absence of sgRNA. Therefore, it appears that the binding mode of AcrIIC4 is different from other reported Acrs, such as AcrVA4, possibly representing a new interaction mode between Acr and CRISPR effector.

In comparison to the RNP structure, stem loop 1 is shifted outward in the presence of AcrIIC4 (Supplementary

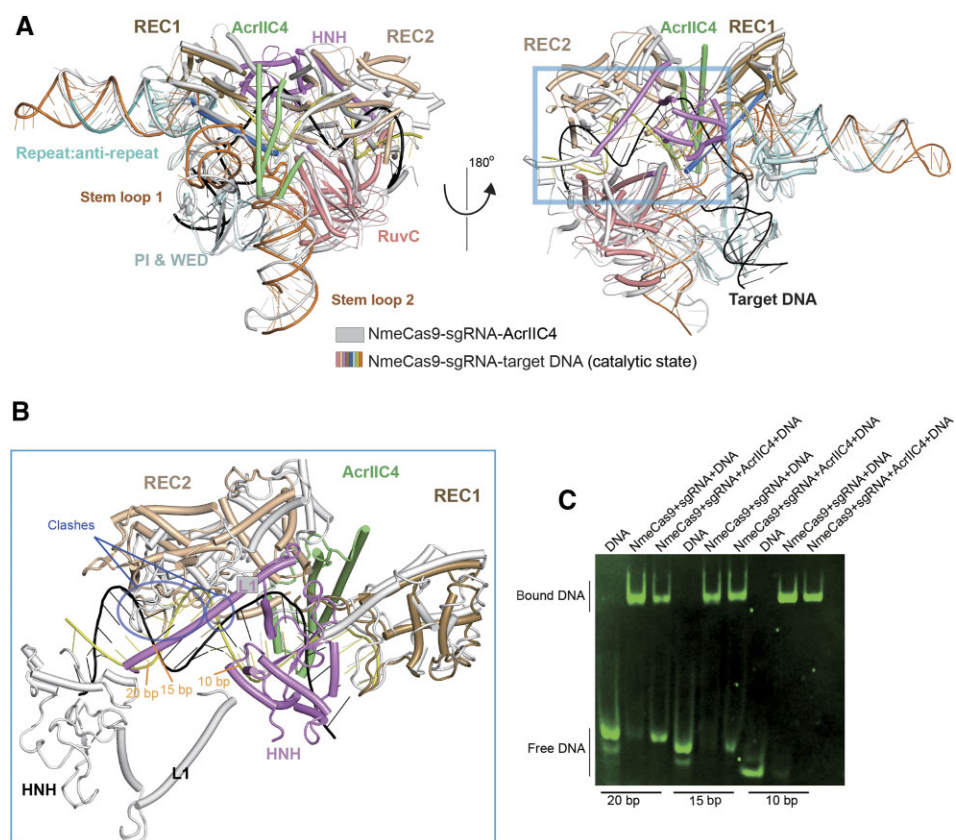


Figure 4. Inhibition mechanism of AcrIIC4. (A) Superimposition of the AcrIIC4-bound NmeCas9-sgRNA ternary structure with NmeCas9-sgRNA-dsDNA ternary complex (catalytic state, PDB:6JDV). (B) Structural comparisons reveal significant clashes between the REC2 domain and the PAM-distal duplex in the presence of AcrIIC4 (highlighted in a big blue circle). The steric clash observed between the L1 linker region and REC2 domain is marked with a small blue circle according to the structural alignment. (C) DNA EMSA assays performed in the presence or absence of AcrIIC4 using target DNA of different lengths. Three independent replicate experiments were conducted.

Figure S5A). Additionally, about half of the repeat: anti-repeat duplex, clamped by REC1 and WED domains, remains unchanged, while the other half undergoes a ~ 6 Å movement upon AcrIIC4 binding (Supplementary Figure S5A). However, the altered portion of the repeat: anti-repeat duplex, with few contacts to NmeCas9, is reported to be dispensable for the endonuclease activity of NmeCas9 (35). Thus, it is suggested that the AcrIIC4-induced allosteric conformational changes of the repeat: anti-repeat duplex have little impact on NmeCas9 activity. Similarly, an allosteric movement is also observed at the end of the stem loop 2 distal to NmeCas9 (Supplementary Figure S5A), implying a nonessential role of this conformational change in modulating NmeCas9 activity.

The inhibitory mechanisms utilized by type II anti-CRISPR proteins can be summarized in several ways. One common mechanism involves the inhibition of sgRNA or target DNA binding. For example, AcrIIA17 and AcrIIC2 hinder the Cas9-sgRNA binary complex formation by interacting with the BH domain of Cas9 (16,40,41). The PAM-binding site of Cas9 can also be occupied by Acrs, such as AcrIIA2, AcrIIA4 and AcrIIC5, thus preventing the binding of target DNA to Cas9 (17,34,42,43). Among these Acrs, AcrIIA4 has been developed to control SpyCas9 activity in zebrafish embryos and mammalian cells (44–46).

Another prevalent strategy involves the physical interaction with the catalytic domains of Cas9, such as the HNH domain. Interestingly, both AcrIIC1 and AcrIIC3 are found to engage the HNH domain to inhibit NmeCas9, albeit with distinct binding modes (14,41). AcrIIC3 has been used to modulate the Nme2Cas9-mediated genome editing in mice (47). In addition, the enzymatic inhibition mechanism is also found in type II Acrs (40,48).

AcrIIC4 recognizes both the REC lobe and sgRNA to lock the REC2 domain, thereby preventing the conformational rearrangements required for NmeCas9 activity. This mechanism is different from the aforementioned type II Acr mechanisms. Interestingly, AcrIIC3 is also reported to interact with the REC2 domain (14,41); however, the binding mode of AcrIIC3 to REC2 is distinct from that of AcrIIC4. AcrIIC3 specifically binds to a region of REC2 that is located distal to REC1, whereas AcrIIC4 contacts a region of REC2 that is located proximal to the REC1 domain. More importantly, the inhibition of NmeCas9 by AcrIIC3 appears to be predominantly accomplished through trapping the HNH domain rather than the REC2 domain. Altogether, our results bring new insights into the inhibitory mechanisms of Acr proteins and provide a basis for the development of Acr proteins in gene editing applications.

DATA AVAILABILITY

The atomic coordinates and cryo-EM map have been deposited in the Protein Data Bank under the accession codes 7XVQ (crystal structure of apo AcrIIC4), 8JA0/EMDB-36123 (NmeCas9-sgRNA-AcrIIC4 ternary complex), respectively.

SUPPLEMENTARY DATA

Supplementary Data are available at NAR Online.

ACKNOWLEDGEMENTS

We thank the staffs from BL17B/BL18U1/BL19U1/BL19U2/BL01B beamlines of the National Facility for Protein Science in Shanghai at Shanghai Synchrotron Radiation Facility, for assistance during data collection.

Author contributions: H.Y. and G.Y. conceived the study. F.L., J.G., and G.S. carried out the molecular cloning, protein expression and purification, H.Y., F.L., J.G. and G.S. performed the biochemical assays with help from N.J., X.L., X.W. and Y.W. G.S., F.L., J.W. and J.H. performed the protein crystallization with the guidance from H.Y. and H.Z. X.L. and built the atomic models. C.Z., Z.L. and G.Y. processed the cryo-EM data and X.L. built the atomic model. X.L., G.Y. and H.Y. wrote the manuscript with contributions from the other authors.

FUNDING

National Key R&D Program of China [2022YFC3400400 to Y.W. and 2022YFA0911800 to Z.L.]; National Natural Science Foundation of China [32200496 to G.Y. and 32201004 to Z.L.]; Scientific Research Program of Tianjin Municipal Education Commission [2022KJ192 to H.Y.]; Hubei Provincial Natural Science Foundation [ZRMS2022000096 to Z.L.]; Scientific Research Program of Hubei Provincial Department of Education. Funding for open access charge: National Natural Science Foundation of China [32200496 to G.Y. and 32201004 to Z.L.]; Ministry of Science and Technology [2022YFA0911800 to Z.L.]; Hubei Provincial Natural Science Foundation [ZRMS2022000096 to Z.L.].

Conflict of interest statement. None declared.

REFERENCES

- Hampton, H.G., Watson, B.N.J. and Fineran, P.C. (2020) The arms race between bacteria and their phage foes. *Nature*, **577**, 327–336.
- Makarova, K.S., Wolf, Y.I., Iranzo, J., Shmakov, S.A., Alkhnbashi, O.S., Brouns, S.J.J., Charpentier, E., Cheng, D., Haft, D.H., Horvath, P. *et al.* (2020) Evolutionary classification of CRISPR-Cas systems: a burst of class 2 and derived variants. *Nat. Rev. Micro.*, **18**, 67–83.
- Shmakov, S., Smargon, A., Scott, D., Cox, D., Pyzocha, N., Yan, W., Abudayyeh, O.O., Gootenberg, J.S., Makarova, K.S., Wolf, Y.I. *et al.* (2017) Diversity and evolution of class 2 CRISPR-Cas systems. *Nat. Rev. Micro.*, **15**, 169–182.
- Shmakov, S., Abudayyeh, O.O., Makarova, K.S., Wolf, Y.I., Gootenberg, J.S., Semenova, E., Minakhin, L., Joung, J., Konermann, S., Severinov, K. *et al.* (2015) Discovery and functional characterization of diverse class 2 CRISPR-Cas systems. *Mol. Cell*, **60**, 385–397.
- Lapinaite, A., Knott, G.J., Palumbo, C.M., Lin-Shiao, E., Richter, M.F., Zhao, K.T., Beal, P.A., Liu, D.R. and Doudna, J.A. (2020) DNA capture by a CRISPR-Cas9-guided adenine base editor. *Science*, **369**, 566–571.
- Park, S.H., Lee, C.M., Dever, D.P., Davis, T.H., Camarena, J., Srifa, W., Zhang, Y., Paikari, A., Chang, A.K., Porteus, M.H. *et al.* (2019) Highly efficient editing of the beta-globin gene in patient-derived hematopoietic stem and progenitor cells to treat sickle cell disease. *Nucleic Acids Res.*, **47**, 7955–7972.
- Schmidt, M.J., Gupta, A., Bednarski, C., Gehrig-Giannini, S., Richter, F., Pitzler, C., Gamalinda, M., Galonska, C., Takeuchi, R., Wang, K. *et al.* (2021) Improved CRISPR genome editing using small highly active and specific engineered RNA-guided nucleases. *Nat. Commun.*, **12**, 4219.
- Ibraheem, R., Song, C.Q., Mir, A., Amrani, N., Xue, W. and Sontheimer, E.J. (2018) All-in-one adeno-associated virus delivery and genome editing by *Neisseria meningitidis* Cas9 in vivo. *Genome Biol.*, **19**, 137.
- Hoffmann, M.D., Mathony, J., Upmeyer Zu Belzen, J., Harteveld, Z., Aschenbrenner, S., Stengl, C., Grimm, D., Correia, B.E., Eils, R. and Niopek, D. (2021) Optogenetic control of *Neisseria meningitidis* Cas9 genome editing using an engineered, light-switchable anti-CRISPR protein. *Nucleic Acids Res.*, **49**, e29.
- Amrani, N., Gao, X.D., Liu, P., Edraki, A., Mir, A., Ibraheem, R., Gupta, A., Sasaki, K.E., Wu, T., Donohoue, P.D. *et al.* (2018) NmeCas9 is an intrinsically high-fidelity genome-editing platform. *Genome Biol.*, **19**, 214.
- Marino, N.D., Pinilla-Redondo, R., Csorgo, B. and Bondy-Denomy, J. (2020) Anti-CRISPR protein applications: natural brakes for CRISPR-Cas technologies. *Nat. Methods*, **17**, 471–479.
- Peng, X., Mayo-Munoz, D., Bhoobalan-Chitty, Y. and Martinez-Alvarez, L. (2020) Anti-CRISPR Proteins in Archaea. *Trends Microbiol.*, **28**, 913–921.
- Jia, N. and Patel, D.J. (2021) Structure-based functional mechanisms and biotechnology applications of anti-CRISPR proteins. *Nat. Rev. Mol. Cell Biol.*, **22**, 563–579.
- Harrington, L.B., Doxzen, K.W., Ma, E., Liu, J.J., Knott, G.J., Edraki, A., Garcia, B., Amrani, N., Chen, J.S., Cofsky, J.C. *et al.* (2017) A Broad-Spectrum Inhibitor of CRISPR-Cas9. *Cell*, **170**, 1224–1233.
- Mathony, J., Harteveld, Z., Schmela, C., Upmeyer Zu Belzen, J., Aschenbrenner, S., Sun, W., Hoffmann, M.D., Stengl, C., Scheck, A., Georgeson, S. *et al.* (2020) Computational design of anti-CRISPR proteins with improved inhibition potency. *Nat. Chem. Biol.*, **16**, 725–730.
- Thavalingam, A., Cheng, Z., Garcia, B., Huang, X., Shah, M., Sun, W., Wang, M., Harrington, L., Hwang, S., Hidalgo-Reyes, Y. *et al.* (2019) Inhibition of CRISPR-Cas9 ribonucleoprotein complex assembly by anti-CRISPR AcrIIC2. *Nat. Commun.*, **10**, 2806.
- Sun, W., Zhao, X., Wang, J., Yang, X., Cheng, Z., Liu, S., Wang, J., Sheng, G. and Wang, Y. (2023) Anti-CRISPR AcrIIC5 is a dsDNA mimic that inhibits type II-C Cas9 effectors by blocking PAM recognition. *Nucleic Acids Res.*, **51**, 1984–1995.
- Lee, J., Mir, A., Edraki, A., Garcia, B., Amrani, N., Lou, H.E., Gainetdinov, I., Pawluk, A., Ibraheem, R., Gao, X.D. *et al.* (2018) Potent Cas9 inhibition in bacterial and human cells by AcrIIC4 and AcrIIC5 anti-CRISPR proteins. *Mbio*, **9**, e02321-18.
- Kim, G.E., Lee, S.Y. and Park, H.H. (2021) Crystal structure of the anti-CRISPR, AcrIIC4. *Protein Sci.*, **30**, 2474–2481.
- Hwang, S., Pan, C., Garcia, B., Davidson, A.R., Moraes, T.F. and Maxwell, K.L. (2022) Structural and mechanistic insight into CRISPR-Cas9 inhibition by anti-CRISPR protein AcrIIC4(Hpa). *J. Mol. Biol.*, **434**, 167420.
- Vonrhein, C., Flensburg, C., Keller, P., Sharff, A., Smart, O., Paciorek, W., Womack, T. and Bricogne, G. (2011) Data processing and analysis with the autoPROC toolbox. *Acta Crystallogr. D Biol. Crystallogr.*, **67**, 293–302.
- Wang, N., Wang, M., Gao, Y., Ran, T., Lan, Y., Wang, J., Xu, L. and Wang, W. (2012) Crystallization and preliminary X-ray crystallographic analysis of a blue-light-absorbing proteorhodopsin. *Acta Crystallogr. Sect. F Struct. Biol. Cryst. Commun.*, **68**, 281–283.
- Zhang, W.-Z., Tang, J.-C., Wang, S.-S., Wang, Z.-J., Qin, W.-M. and He, J.-H. (2019) The protein complex crystallography beamline (BL19U1) at the Shanghai Synchrotron Radiation Facility. *Nucl. Sci. Tech.*, **30**, 170.

24. Minor, W., Cymborowski, M., Otwinowski, Z. and Chruszcz, M. (2006) HKL-3000: the integration of data reduction and structure solution—from diffraction images to an initial model in minutes. *Acta Crystallogr. D Biol. Crystallogr.*, **62**, 859–866.
25. Adams, P.D., Grosse-Kunstleve, R.W., Hung, L.W., Ioerger, T.R., McCoy, A.J., Moriarty, N.W., Read, R.J., Sacchettini, J.C., Sauter, N.K. and Terwilliger, T.C. (2002) PHENIX: building new software for automated crystallographic structure determination. *Acta Crystallogr. D Biol. Crystallogr.*, **58**, 1948–1954.
26. Mirdita, M., Schütze, K., Moriawaki, Y., Heo, L., Ovchinnikov, S. and Steinegger, M. (2022) ColabFold: making protein folding accessible to all. *Nat. Methods*, **19**, 679–682.
27. Emsley, P. and Cowtan, K. (2004) Coot: model-building tools for molecular graphics. *Acta Crystallogr. D Biol. Crystallogr.*, **60**, 2126–2132.
28. Afonine, P.V., Grosse-Kunstleve, R.W., Echols, N., Headd, J.J., Moriarty, N.W., Mustyakimov, M., Terwilliger, T.C., Urzhumtsev, A., Zwart, P.H. and Adams, P.D. (2012) Towards automated crystallographic structure refinement with phenix.refine. *Acta Crystallogr. D Biol. Crystallogr.*, **68**, 352–367.
29. Thompson, R.F., Iadanza, M.G., Hesketh, E.L., Rawson, S. and Ranson, N.A. (2019) Collection, pre-processing and on-the-fly analysis of data for high-resolution, single-particle cryo-electron microscopy. *Nat. Protoc.*, **14**, 100–118.
30. Zivanov, J., Nakane, T., Forsberg, B.O., Kimanius, D., Hagen, W.J., Lindahl, E. and Scheres, S.H. (2018) New tools for automated high-resolution cryo-EM structure determination in RELION-3. *Elife*, **7**, e42166.
31. Zheng, S.Q., Palovcak, E., Armache, J.P., Verba, K.A., Cheng, Y. and Agard, D.A. (2017) MotionCor2: anisotropic correction of beam-induced motion for improved cryo-electron microscopy. *Nat. Methods*, **14**, 331–332.
32. Zhang, K. (2016) Gctf: real-time CTF determination and correction. *J. Struct. Biol.*, **193**, 1–12.
33. Punjani, A., Rubinstein, J.L., Fleet, D.J. and Brubaker, M.A. (2017) cryoSPARC: algorithms for rapid unsupervised cryo-EM structure determination. *Nat. Methods*, **14**, 290–296.
34. Liu, L., Yin, M., Wang, M. and Wang, Y. (2019) Phage AcrIIA2 DNA mimicry: structural basis of the CRISPR and anti-CRISPR Arms Race. *Mol. Cell*, **73**, 611–620.
35. Sun, W., Yang, J., Cheng, Z., Amrani, N., Liu, C., Wang, K., Ibraheim, R., Edraki, A., Huang, X., Wang, M. *et al.* (2019) Structures of *Neisseria meningitidis* Cas9 complexes in catalytically poised and anti-CRISPR-inhibited states. *Mol. Cell*, **76**, 938–952.
36. Jiang, F. and Doudna, J.A. (2017) CRISPR-Cas9 structures and mechanisms. *Annu. Rev. Biophys.*, **46**, 505–529.
37. Bravo, J.P.K., Liu, M.S., Hibshman, G.N., Dangerfield, T.L., Jung, K., McCool, R.S., Johnson, K.A. and Taylor, D.W. (2022) Structural basis for mismatch surveillance by CRISPR-Cas9. *Nature*, **603**, 343–347.
38. Zhang, H., Li, Z., Dackowski, C.M., Gabel, C., Mesecar, A.D. and Chang, L. (2019) Structural basis for the inhibition of CRISPR-Cas12a by anti-CRISPR proteins. *Cell Host Microbe*, **25**, 815–826.
39. Peng, R., Li, Z., Xu, Y., He, S., Peng, Q., Wu, L.A., Wu, Y., Qi, J., Wang, P., Shi, Y. *et al.* (2019) Structural insight into multistage inhibition of CRISPR-Cas12a by AcrVA4. *Proc. Natl. Acad. Sci. USA*, **116**, 18928–18936.
40. Wang, X., Li, X., Ma, Y., He, J., Liu, X., Yu, G., Yin, H. and Zhang, H. (2022) Inhibition mechanisms of CRISPR-Cas9 by AcrIIA17 and AcrIIA18. *Nucleic Acids Res.*, **50**, 512–521.
41. Zhu, Y., Gao, A., Zhan, Q., Wang, Y., Feng, H., Liu, S., Gao, G., Serganov, A. and Gao, P. (2019) Diverse mechanisms of CRISPR-Cas9 inhibition by type IIC anti-CRISPR proteins. *Mol. Cell*, **74**, 296–309.
42. Yang, H. and Patel, D.J. (2017) Inhibition mechanism of an anti-CRISPR suppressor AcrIIA4 targeting SpyCas9. *Mol. Cell*, **67**, 117–127.
43. Hwang, S., Shah, M., Garcia, B., Hashem, N., Davidson, A.R., Moraes, T.F. and Maxwell, K.L. (2023) Anti-CRISPR protein AcrIIC5 inhibits CRISPR-Cas9 by occupying the target DNA binding pocket. *J. Mol. Biol.*, **435**, 167991.
44. Takasugi, P.R., Wang, S., Truong, K.T., Drage, E.P., Kanishka, S.N., Higbee, M.A., Bamidele, N., Ojelabi, O., Sontheimer, E.J. and Gagnon, J.A. (2022) Orthogonal CRISPR-Cas tools for genome editing, inhibition, and CRISPR recording in zebrafish embryos. *Genetics*, **220**, iyab196.
45. Shin, J., Jiang, F., Liu, J.J., Bray, N.L., Rauch, B.J., Baik, S.H., Nogales, E., Bondy-Denomy, J., Corn, J.E. and Doudna, J.A. (2017) Disabling Cas9 by an anti-CRISPR DNA mimic. *Sci. Adv.*, **3**, e1701620.
46. Bubeck, F., Hoffmann, M.D., Harteveld, Z., Aschenbrenner, S., Bietz, A., Waldhauer, M.C., Borner, K., Fakhiri, J., Schmela, C., Dietz, L. *et al.* (2018) Engineered anti-CRISPR proteins for optogenetic control of CRISPR-Cas9. *Nat. Methods*, **15**, 924–927.
47. Lee, J., Mou, H., Ibraheim, R., Liang, S.Q., Liu, P., Xue, W. and Sontheimer, E.J. (2019) Tissue-restricted genome editing in vivo specified by microRNA-repressible anti-CRISPR proteins. *RNA*, **25**, 1421–1431.
48. Ka, D., An, S.Y., Suh, J.Y. and Bae, E. (2018) Crystal structure of an anti-CRISPR protein, AcrIIA1. *Nucleic Acids Res.*, **46**, 485–492.